ChemPubSoc Europe

DOI: 10.1002/cphc.201300126

A New Approach for the Simulation of Electrochemiluminescence (ECL)

Oleksiy V. Klymenko,[a, b] Irina Svir,*[a, b] and Christian Amatore*[a]

Dedicated to Adam Heller, a dear friend and great colleague, and most of all a visionary who had the will and skills to make his dreams come true

The validity and accuracy of our new numerical approach implemented in KISSA-1D software when applied to a theoretical study of different types of electrochemiluminescence (ECL) is established by comparison with existing analytical solutions and others specifically derived in this work, as well as with independent numerical solutions obtained by using commercial software. The efficiency and comprehensiveness of this approach are illustrated by using a representative series of published ECL reaction schemes taken as typical case studies when ECL is generated by a single electrode under amperometric or voltammetric conditions, even when rate constants used in the simulations far exceed any of their realistic experimental limits.

1. Introduction

Electrochemical reaction mechanisms leading to electrochemiluminescence (ECL) have attracted significant interest for fundamental reasons related to photochemistry and physical electrochemistry and also for analytical purposes. ECL belongs to the general class of chemiluminescence in which a would-be highly exergonic electron transfer (ET) is kinetically shunted by a much less exergonic one, leading to an electronically excited state, S*. The latter deactivates in part through emission of a photon with an energy value close to that of the difference in enthalpies. As such, it can be said that ECL is an extremely suitable method for probing the Marcus inverted region through competition between ET towards fundamental states versus ET towards excited product states.

To the best of our knowledge, the first type of ECL reaction mechanisms investigated involved annihilation ECL,[1] in which an oxidised and a reduced species, both generated sequentially in time at the same working electrode surface by fast specific potential modulation, react in solution to form an excited state prone to emit light upon returning to its ground state. This type of mechanism helped to improve the fundamental understanding of highly energetic outer-sphere ET reactions. A second kind of ECL reaction mechanism was discovered in the late 1970s. It involved an inert luminophore parent molecule, the reaction of which (or that of its reduced or oxidised form) with species resulting from reduction or oxidation of a co-reactant (respectively) produced a reaction cascade, leading ultimately to deactivation of the excited state through photon emission.[1] This second approach was rapidly adopted for analytical detection of minute quantities of analytes prone to interfere in its mechanism to modulate the light-intensity output. Indeed, ECL detection is particularly suited to very low detection limits. This stems from the fact that it operates at exceptionally low noise levels because the electrical input (i.e. the electrochemical trigger) is practically decoupled from the optical output (i.e. the ECL yield), which precludes the transmission of significant electrical noise.

Both approaches involve a sequence of extremely rapid second-order reactions (one or more) occurring in the diffusion layer followed by a very fast first-order emissive decay of the extremely short-lived electronically excited state(s), S*. Therefore, the overall concentration of the emitting species is vanishingly small; this situation poses important difficulties for mathematical modelling of ECL reaction mechanisms. Indeed, the variation of such small concentrations in space and time is critical for the prediction of the ECL light intensity. Furthermore, theoretical investigations of such an intrinsically difficult electrochemical problem may be complicated by other distinctive features borne either by discontinuities of fluxes (because of rapid stepwise changes of potential at the electrode/solution interface) or by the necessity of simultaneously handling extremely different time and space scales (e.g. extremely localised high reactions rates compared with smooth diffusion patterns and rates). Except for some specific limits (see below), the models are then generally not amenable to analytical treatments, and thus, must be solved by using numerical methods with an excellent precision and accuracy for predicting vanishingly small concentrations with space and time. This is certainly a heavy-duty numerical obligation, which we have been tackling over a period of time.

Previously, we developed a program called ECL Package[2] for solving the basic mechanism of annihilation-type ECL on

[a] Dr. O. V. Klymenko, Dr. I. Svir, Dr. C. Amatore
Département de Chimie, Ecole Normale Supérieure
24 rue Lhomond, 75005 Paris (France)
E-mail: irina.svir@ens.fr
christian.amatore@ens.fr

[b] Dr. O. V. Klymenko, Dr. I. Svir
Mathematical & Computer Modelling laboratory
Kharkov National University of Radio Electronics
14 Lenin Avenue, Kharkov, 61166 (Ukraine)

working (micro)electrodes of different geometries (planar, sphere, band, channel double band and disk). The main aim of this work consisted of accurately simulating the corresponding non-linear problem at microelectrodes under different mass-transport conditions when taking into account edge effects at disk and band electrodes. Indeed, drastically uneven distributions of current flux lines affect local concentrations equally with grave consequences for the local rate of bimolecular reactions, and hence, the photon flux in ECL annihilation mechanisms. To this end, several different approaches were implemented, including coordinate transformations and non-uniform simulation meshes specifically designed to resolve the problem of edge effects with high accuracy, while using the minimum number of grid nodes (to minimise computational costs) for the reaction mechanism considered. Thus, ECL annihilation was used as a test problem for finding optimal numerical methods and grid-generation algorithms,[2,3] including some conformal mappings for different shapes of electrodes (sphere, disk).[4]

Owing to great interest in precise simulations of these kinds of mechanistic situations, other numerical approaches have been developed over the years. Two of them need special emphasis owing to their use in the electrochemical community. The first, DigiSim,[5a] which is a finite-differences-based program, is generally considered to be a prototype of versatile simulation programs for predicting current–potential–time relationships for complex electrochemical sequences. It relies on exponential spatial compression near an electrode surface to increase the precision in computing currents when thin kinetic layers form near the electrode over dimensions much smaller than the time-expanding diffusion layer. This is certainly fine for classical families of fast EC mechanisms, although exponential compression should be handled with great care, but is not adapted to situations similar to those that occur in EE-type mechanisms or in ECL annihilation because the critical kinetic layer is now located far from the electrode, spanning a very thin solution zone and moving with time (reaction front). However, DigiSim software may be used to circumvent such difficulties under specific circumstances by indirectly modelling ECL annihilation photon fluxes through a numerical approximation that amounts to treating emitted photons as very rapidly diffusing electroactive species.[5b] This allows ECL intensity to be numerically computed as the equivalent flux of these pseudo-photons through the electrode surface.[5b]

Another strategy consists of using multi-purpose finite-element method (FEM) software, such as Comsol,[6] which has become a popular simulation tool among electrochemists. Providing its mathematical programming (namely, definition of the model, computational grid and method parameters) is performed correctly, which requires some expertise because Comsol was not designed to handle the very specific electrochemical boundary and kinetic conditions readily, such a multi-purpose program generally produces good predictions. Indeed, it offers the option of numerically auto-adapted spatial FEM grids that generally conform well to the problem at hand. Yet, because such grids are implemented through numerical auto-adaptation, precision may fail under several classical electrochemical conditions,[7] in particular, when several spatial scales have to be handled simultaneously. Skilled users of Comsol may circumvent such difficulties in many cases, but this requires solid expertise and ultimately implies long computation times and memory occupation (see below). In our opinion, even if approaches based on Comsol lead to excellent results under specific circumstances, they rely on profound expertise from their potential users, and hence, may easily lead to erroneous predictions in the hands of novices.

Due to the absence of a specialised computer program that allows the simulation of any reaction mechanism leading to ECL, researchers have also resorted to the combined use of specialised and general-purpose software. Thus, Sartin et al. employed DigiElch (a successor of DigiSim) to simulate voltammetric responses and Comsol to obtain concentration distributions of two light-emitting species, and hence, indirectly evaluate ECL emission intensity.[8]

Conversely, we have developed a new numerical approach implemented in new software, KISSA (for the solution of 1D and 2D electrochemical problems),[9,10] which enables efficient numerical simulation of any electrochemical reaction mechanisms that may comprise of any sequence of hetero- and homogeneous ET sequences coupled through homogeneous mono- and/or bimolecular reactions involving rate constants that greatly exceed any experimentally realistic ones (i.e. up to a few $10^{12}\,s^{-1}$ and $10^{11}\,M^{-1}\,s^{-1}$, respectively). This was implemented more recently to incorporate the effect of natural convection,[11,12] pre-scan conditioning of the electrode[12] and generalised Laviron's mechanisms that involve free and adsorbed species.[13]

The success of this approach rests on the simultaneous implementation of specific conformal mappings of the space to accommodate all usual electrode and nano-/microelectrode geometries (such as planar, spherical, disk, cylindrical, band and double band),[9c,d] and of a specifically developed and original kinetic criterion for adaptive tracking of rapid concentration changes and/or fronts of fast homogeneous reactions, which may travel in the bulk solution during the course of the experiment.[9a,b] Such implementations do not require any input from users, who need only define the electrochemical system and a sequence of redox and chemical steps. This ensures accurate solutions for both electrochemical currents (fluxes) and concentration distributions to be obtained, even for species that are so reactive that their vanishingly small concentrations are spatially restricted to extremely thin reaction fronts or kinetic layers.

Such complex situations are evidently fully integrated into the different ECL mechanisms described above. Herein, we present a specialised version of this approach to ECL kinetics, to offer potential users a new, original and highly precise method that is able to handle extremely difficult numerical situations without the necessity for long computational times and memory occupation, as well as specific attention from users. We first establish the validity, precision and accuracy of the present approach through comparing its results to analytical limits, which may be derived for seminal ECL mechanisms when operated under drastic kinetic conditions, creating the

most stringent circumstances for any digital simulations. The advantages of this approach are then documented through typical simulations of the three main ECL generation mechanisms.

2. Results and Discussion

2.1. Description and Validation of the Approach

The main framework of the present approach relies on two simultaneous strategies, the implementation of which is automatic and does not require specific decisions from the user. This first involves specific mathematical (quasi)conformal mappings of the space to adapt simulation grids to the characteristic problem imposed by the specific geometry of the working electrode. A variety of such conformal transformations have been reported by us over the years to accommodate the main types of metallic solid or liquid micro-/nanoelectrodes used nowadays in electrochemical laboratories, namely, planar, spherical, cylindrical, disk and band, including purposely or accidentally recessed or protruding ones and their assemblies. This is coupled to a second auto-adaptive strategy that detects, at each time step, all spatial ranges within the diffusion layer in which kinetic terms may equal or exceed a specified numerical constraint. In such ranges lying near the electrode surface (i.e. classical kinetic layers) or anywhere within the diffusion layer (i.e. reaction fronts), the spatial grid is compressed, so that the magnitude of the local kinetic terms can be handled without compromising the precision and accuracy of the ensuing concentration values at the next time step, regardless of the magnitude or confinement of their spatial variations. Several previous auto-adaptive strategies were proposed or used (e.g. in Comsol), but, to the best of our knowledge, most of them relied on a previous estimation of local concentration gradients, that is, they required a pre-integration based on a possibly non-fitted grid (i.e. that fitted to the previous time iteration step), and thus, may have required several iterations, hence long computation times. Conversely, the approach introduced in KISSA (1D, 2D) relies on the concept of "pure kinetics (KP)" introduced by Savéant's group,[14] that is, only the local magnitudes of the chemical kinetic terms are considered, so that it ensures perfect adaptation of the grid to the kinetic problem.

Coupling of the two approaches allows the number of mesh grid points to be decreased, where the problem is readily handled by the conformal map only, and the mesh point density to be increased, where high kinetic terms are involved, regardless of the finite difference algorithm used (several modifications of implicit schemes were implemented by the developers of KISSA).[9] This is performed at each time step, so that the simulation grid literally tracks the kinetic difficulties with time. Finally, owing to the ensuing precision, the time grid may also be uneven and expanded or compressed as a function of the simulated experiment duration or of sharp variations in the electrode potential (i.e. scan inversion in voltammetry and step sequence of potentials in chronoamperometry). This novel procedure reduces computational times for identical precision and, most of all, avoids oscillations at initial and switch potentials when pulsed-potential methods are investigated.

Overall, this produces precise and accurate simulations of concentration profiles (not only for their gradients at the electrode) with relatively short computation times and small memory occupation. These great advantages are thus perfectly suited to eliminate important simulation difficulties borne by ECL mechanisms, as established below through considering Schemes 1 and 2, which exemplify two representative ECL sequences, that is, ECL annihilation (Scheme 1) or ECL generation through a luminophore and a co-reactant (Scheme 2). Notably, a wider variety of ECL sequences may result from combinations of different routes for the generation of excited species. We retain Schemes 1 and 2 because they illustrate different experimental situations that lead to the species involved in the ET steps [Eqs. (3) and (7)], depending on whether they originate from the same precursor [Eq. (3)] or from two distinct precursors, possibly at different concentrations [Eq. (7)]. Scheme 3, which is presented later, examines another kind of situation, in which ECL ultimately follows the oxidation of only one species (namely, TPrA) [Eqs. (26)–(36)].

$$A - e \rightleftharpoons A^+ \quad (1)$$

$$A + e \rightleftharpoons A^- \quad (2)$$

$$A^+ + A^- \xrightarrow{k^{ET}} \varepsilon A^* + (2-\varepsilon)A \quad (3)$$

$$A^* \xrightarrow{k^{ECL}} A + \gamma h\nu \quad (4)$$

Scheme 1. ECL-annihilation.

$$A - e \rightleftharpoons A^+ \quad (5)$$

$$B + e \rightleftharpoons B^- \quad (6)$$

$$A^+ + B^- \xrightarrow{k^{ET}} \varepsilon A^{3*} + (1-\varepsilon)A + B \quad (7)$$

$$2\,A^{3*} \xrightarrow{k^{T\rightarrow S}} \chi A^* + (2-\chi)A \quad (8a)$$

$$A^* \xrightarrow{k^{ECL}} A + \gamma h\nu \quad (9a)$$

or:

$$2\,A^{3*} \xrightarrow{k^{T\rightarrow S}} A_2^* \quad (8b)$$

$$A_2^* \xrightarrow{k^{ECL}} 2A + \gamma h\nu \quad (9b)$$

Scheme 2. "Mixed ECL".

In Schemes 1 and 2, the photon-emitting species is the extremely transient singlet excited state, A^*, the concentration of which must be simulated with extreme care because at each instant the overall photon flux is given by Equation (10):

$$I_{ECL}(t) = \phi_{ECL} k^{ECL} \int_V [A^*](t) dV \quad (10)$$

in which ϕ_{ECL} is the overall quantum yield, t is the time and V is the volume of the light collection optical pathway across the cell. For Scheme 1, $\phi_{ECL} = \Gamma\gamma\varepsilon$, whereas $\phi_{ECL} = \Gamma\gamma\varepsilon\chi$ for Scheme 2, and Γ is a geometrical capture and collection efficiency factor, the value of which depends on the experimental arrangement, optical path and efficiency of photomultiplier used. Equation (10) crystallises all of the numerical difficulty at hand. Indeed, $[A^*](t)$ is an extremely minute quantity as soon as k^{ECL} is extremely large, although the integral is over the whole optical pathway. Hence, any slight numerical error or bias in the evaluation of $[A^*](t)$ may result in incorrect predictions of $I_{ECL}(t)$. In other words, the dependence of $[A^*](t)$ on the position in the cell must be simulated with extremely high precision and accuracy, and the numerical problem is the hardest when this concentration is vanishingly small, that is, in the long-time limit. For this reason, we wish to test the results simulated with the present approach under such drastic conditions to stress its validity.

In doing so, we consider situations that are not likely to be observed experimentally because generally most reactions in Equations (4), (8) or (9) are faster than those in Equations (3) or (7); the last of which are already much faster than the experimental timescales, which applies as soon as $k^{ET} c_0 t \geq 10^3$,[15,16] in which c_0 is the bulk concentration of A and B (in Scheme 2), and which is often true owing to the large concentrations of reduced and oxidised reactants versus those of excited states and because these steps are highly exergonic. Yet, we chose to examine such exceptional conditions because they are more severe than any of those met in usual ECL problems and are those to best illustrate the precision and accuracy of our approach. Furthermore, under these kinetic conditions, the sequences in Schemes 1 and 2 may be amenable to analytical expressions for $I_{ECL}(t)$ (see "Analytical Solutions" Section) in the most kinetically difficult case, in which one considers a double-step chronoamperometric experiment with a first cathodic potential step (i.e. generating a stable A^- or B^- moiety accordingly) of infinite duration, while the second is performed anodically to generate A^+ during time t (note that this is tantamount to performing only the anodic step in a bulk solution of A^- or B^- accordingly).

Thus, one obtains Equation (11) for Scheme 1 (see "Analytical Solutions" Section):

$$\frac{I_{ECL}}{2\Gamma c_0 S\sqrt{Dk^{ECL}}} = \frac{e^{-\eta^2}}{\sqrt{\pi k^{ECL} t}}\left(1 - e^{-2\eta\sqrt{k^{ECL} t}}\right) \quad (11)$$

in which S is the cross-section area of the optical pathway perpendicular to the planar electrode surface, D is the supposed common diffusion coefficient of all species, c_0 is the bulk concentration of A and constant η is the solution of $\mathrm{erf}(\eta) = 1/2$ (namely, $\eta \approx 0.476936$).

Scheme 2 was examined in its limit when the rate-determining step (rds) is the triplet-to-singlet conversion in Equation (8). In the converse situation, A^{3*} obeys a steady state, so that, under the conditions investigated herein, the distinction between Schemes 1 and 2 collapses from a kinetic point of view and ECL intensity is governed by Equation (11). Because A^{3*} decays by a second-order rate law and A^* by a unimolecular process, the limit considered herein should correspond to the most frequent experimental conditions in which the triplet state decays by a bimolecular process. Then, for Scheme 2 involving any of the two sequences one obtains Equation (12):

$$\frac{I_{ECL}}{\Theta\varepsilon\gamma S c_0\sqrt{k^{T\to S} c_0 D}} = \frac{e^{-\eta^2}}{\sqrt{\pi k^{T\to S} c_0 t}} - 3\left(2\eta\varepsilon^{1/3}\sqrt{k^{T\to S} c_0 t} + \left[6\sqrt{\pi k^{T\to S} c_0 t}\, e^{\eta^2}\right]^{1/3}\right)^{-3} \quad (12)$$

in which $\Theta = \chi$ for the sequence in Equations (8a) and (9a), whereas $\Theta = 1$ for that in Equations (8b) and (9b). Interestingly, at infinite times in all cases, the dimensionless photon intensity, ψ_{ECL}, namely, the expression on the left-hand sides of Equations (11) and (12) varies as $(k^{ECL} t)^{-1/2}$ or $(k^{T\to S} c_0 t)^{-1/2}$ accordingly. Figure 1 establishes that these long asymptotic analytical time limits are perfectly respected by simulations based on the present approach.

Similarly, one may also derive short times analytical limits (see "Analytical Solutions" Section), namely, Equation (13) for Scheme 1:

$$\psi_{ECL}^{short} = \frac{I_{ECL}}{2\varepsilon\gamma c_0 S\sqrt{Dk^{ECL}}} = \left(2e^{-\eta^2} - 1\right)\sqrt{\frac{k^{ECL} t}{\pi}} \quad (13)$$

and Equation (14) for Scheme 2:

$$\psi_{ECL}^{short} = \frac{I_{ECL}}{\Theta\varepsilon\gamma S c_0\sqrt{k^{T\to S} c_0 D}} = 0.2018\sqrt{k^{T\to S} c_0 t} \quad (14)$$

Both predict that the dimensionless ECL intensity grows with time as $(k^{ECL} t)^{1/2}$ or as $(k^{T\to S} c_0 t)^{1/2}$. Figure 1 demonstrates that simulations perfectly agree with these analytical short time limits.

As explained above, these tests were performed under extremely stringent kinetic conditions for Schemes 1 and 2, which together encompass most ECL mechanisms reported to date. Although it must again be stressed that it is doubtful that such stringent conditions may be observed experimentally, they consist of the most challenging ones that may arise during ECL experiments. Therefore, one may consider that the excellent agreement they demonstrate between analytical limits and simulations is tantamount to the great reliability of the present numerical approach rooted in the principles of KISSA-1D. Additional confirmation of the excellent validity of the present simulation was given through comparing its predictions to the previous analytical approximation reported by Feldberg[15] for ECL intensity generated during the second potential step of a stepped chronoamperometric experiment investigating a classical annihilation ECL reaction mechanism (Scheme 1) and limiting analytical solutions by Faulkner[17] for the electrochemical currents and concentration profiles of A

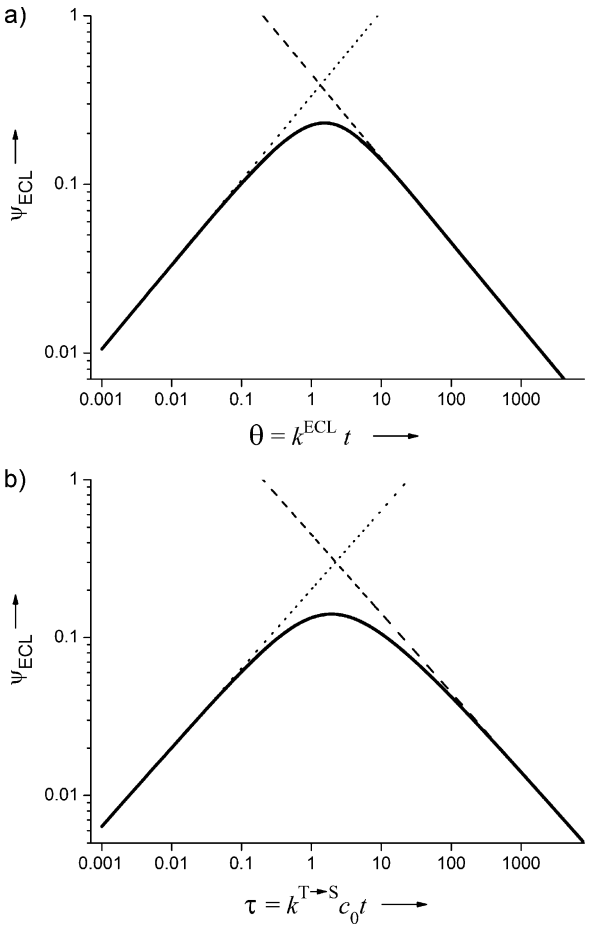

Figure 1. a) Scheme 1. Solid curve: dimensionless ECL intensity variations predicted as a function of $k^{ECL}t$ obtained through simulations with KISSA-1D. Dashed line: analytical limit at infinite times of Equation (11); dotted line: analytical limit at short times [Eq. (13)]. The ECL intensity was considered to be entirely controlled by the decay of A* in Equation (4); this condition applies as soon as $k^{ET}c_0t \geq 10^3$[15,16] owing to the large concentrations of A^- and A^+ versus that of A*. b) Same as in (a), but for Scheme 2 with Equations (8b) and (9b) as a function of $k^{T\rightarrow S}c_0t$, that is, when the triplet bimolecular decay in Equation (8) is the rds. Dashed line: analytical limit at infinite times of Equation (12); dotted line: analytical limit at short times [Eq. (14)]. As in (a), the ECL intensity was evaluated for $k^{ET}c_0t \geq 10^3$.

and B with our notations when the ECL-related steps [i.e. Eqs. (3) and (4) for Scheme 1 or Eqs. (7)–(9) for Scheme 2] are infinitely fast, so that the systems are controlled exclusively by diffusional gradients. Both comparisons (data not shown) again revealed excellent agreement between simulations and the previously published asymptotic analytical approximation and solution [note that the limit of our analytical solution, Eq. (11), at infinite time represents a particular case of Faulkner's analytical solution,[17] corresponding to an infinite duration of the first potential step].

In Section 2.2, we thus wish to exemplify the interest in such an approach through considering several ECL mechanisms reported in the literature,[18–20] which were selected to illustrate the performance of the present simulation approach in the treatment of sharp reaction fronts moving with time within the solution and requiring extremely precise and accurate evaluation of the concentration distributions of all reacting species and especially the emitter species that determine the intensity of the measured ECL signal. All of these examples find their exact counterparts in Schemes 1 or 2, although different electrochemical conditions leading to ECL generation may now be investigated because one is not bound to adapt to those in which analytical limits may be derived.

2.2. Case Studies

Herein, we relied only on published material that was not sufficient to launch a full-scale kinetic analysis. Thus, we scrupulously used the reaction schemes published by their authors as well as thermodynamic and kinetic parameters reported therein. When this was not sufficient to characterise the whole sequence kinetically, we selected rate constants that were realistic in view of general knowledge or indications by the relevant authors to generate kinetic information compatible with the published behaviour accessible to us. It is thus evident that such additional rate constants used in the simulations shown below may not be taken as the result of a full-scale kinetic analysis, but only as appropriate values for our purpose herein and consistent with the information in hand.

2.2.1. Simulation of ECL from the Thianthrene/2,5-Diphenyl-1,3,4-oxadiazole System[18]

This first example involves a reaction cascade initiated by downhill homogeneous ET taking place between electrogenerated thianthrene (TH) cation radicals and 2,5-diphenyl-1,3,4-oxadiazole (PPD) anion radicals.[18] This mechanism, used as a typical mixed ECL experimental system by Bard and Faulkner,[1a] adheres strictly to Scheme 2 [Eqs. (5)–(7), (8a) and (9a), in which A = TH, B = PPD and $\chi = 1$]:[18]

$$TH - e \rightleftharpoons TH^+ \quad (15)$$

$$PPD + e \rightleftharpoons PPD^- \quad (16)$$

$$TH^+ + PPD^- \xrightarrow{k_1} TH^{3*} + PPD \quad (17)$$

$$2\,TH^{3*} \xrightarrow{k_2} TH^* + TH \quad (18)$$

$$TH^* \xrightarrow{k_3} TH + h\nu \quad (19)$$

In ref. [18], Michael and Faulkner investigated the experimental ECL intensity variations generated through a complex potential waveform, involving four sequential steps, as illustrated in the inset of Figure 2a, and reported ECL variations as a function of the dimensionless time duration, $\tau = (t - t_f)/t_f$, in which t_f was the duration of the initial cathodic step that generated PPD^-. This first potential step was followed by a second one of duration $t_0 - t_f$, during which TH^+ was generated and reacted with PPD^-, so that the latter was cleared away from the electrode. A third pulse of duration $t_r - t_0$ was applied to reduce TH^+ in the vicinity of the electrode, but still oxidise PPD^-. The fourth pulse was again anodic to regenerate TH^+ at the electrode surface. Interest in such a complex sequence was to demonstrate that the ECL process was exclusively homogeneous and took place at some distance from the

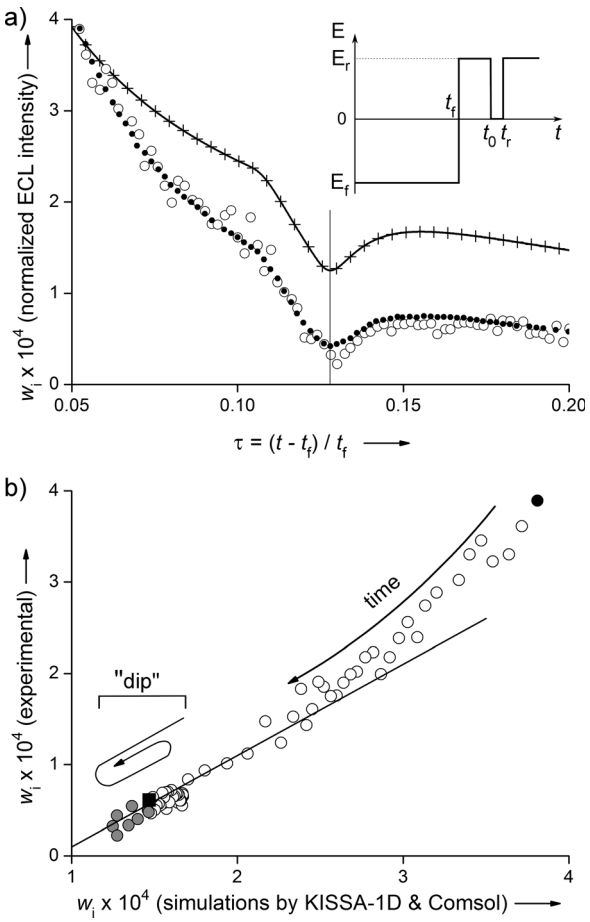

Figure 2. a) Normalised ECL intensity simulated by different approaches [KISSA-1D (solid line) and Comsol (crosses)] and reproduced from ref. [18] [experimental data (open circles) and fitted simulations (dots)]. b) Plot of experimental ECL intensity data (circles) from ref. [18] against simulations by KISSA-1D, for which the start point ($\tau = 0.05$) is shown by a filled circle, the end point ($\tau = 0.2$) by the filled square and points corresponding to the dip in w_i are in grey. The results of the simulation (normalised ECL intensity, $w_i = I_{ECL} t_f^{1/2}/SD^{1/2}c_0$) correspond to the following parameter values: initial concentrations were $[TH]_0 = [PPD]_0 = 1$ mM; diffusion coefficients were $D_{TH} = D_{TH^+} = D_{TH^{\bullet}} = D_{TH^*} = 2.7 \times 10^{-5}$ cm^2 s^{-1} and $D_{PPD} = D_{PPD^-} = 2.6 \times 10^{-5}$ cm^2 s^{-1}; redox reactions parameters were $k_0^{TH} = 1$ cm s^{-1}, $E_{TH}^0 = 1.25$ V and $k_0^{PPD} = 0.14$ cm s^{-1}, $E_{PPD}^0 = -2.17$ V; homogeneous chemical rate constants were $k_1 = k_2 = 10^{10}$ M^{-1} s^{-1}, $k_3 = 10^{10}$ s^{-1}; potential steps: $E_f = -2.5$ V, $t_f = 0.5$ s, $E_r = 1.7$ V, $t_0 = 0.55$ s and $t_r = 0.56$ s; ECL quantum yield $\phi_{ECL} = 2.5 \times 10^{-4}$.

electrode surface within the core of the diffusion layer. Indeed, the diffusional delay required for the concentration changes at the electrode surface to propagate up to the narrow ECL-generating zone, where TH^+ and PPD^- may annihilate each other, showed up as a smooth dip in the ECL intensity over a time window with boundaries that lagged behind the values of t_0 (beginning) and t_r (end). Figure 2 shows that the present approach perfectly reproduces this behaviour and the ECL intensity dip. The predicted ECL intensity correlates very well with the experimental data, although two apparent problems are noted (see Figure 2b). At sufficiently small values of t, the ECL variations are considerably smoother than the experimental ones; this is not really puzzling because such discrepancies are often observed in ECL experiments and are ascribed to the fact that in experiments a fraction of electrogenerated PPD^- and TH^+ may be scavenged by reactions with impurities.[21] More seriously, at sufficiently large values of τ, one obtains, as expected, a good linear correlation with slope unity (owing to the experimental data dispersion) between predictions and experimental data, but involving a constant shift. Because we had no explanation for such a constant shift[1], we decided to compare the present simulated results with those obtained by using Comsol Multiphysics (v. 4.3),[6] since the existence of such a shift was a baffling issue for our present purpose of establishing the validity of our approach. Although this needed about 15 times longer to achieve comparable precision and accuracy as KISSA-1D (namely, 149 vs 9.5 s), Comsol simulations produced identical results to ours, which is evident from Figure 2. Hence, we are confident that the observed shift pertains to the reported experimental data, perhaps involving an improper vertical scale origin in the original figure.

2.2.2. Effect of Natural Convection on Annihilation-Type ECL

In the previous sections we have considered, as in most published theoretical works, that, as soon as no hydrodynamic regime prevails (i.e. as soon as the solution is macroscopically still), diffusion layers may extend up to infinity when the experimental duration increases. Hence, most electrochemical models consider that all chemical and electrochemical phenomena are governed by diffusion-reaction processes. In typical experiments, however, this is not true as was recognised by Nernst when he introduced his concept of the "Nernst diffusion layer". This concept was revisited some years ago based on Levich's seminal views of solution spontaneous hydrodynamics near wall boundaries and a physicochemically correct model of this phenomenon could be established ("natural convection layer")[11a] and validated experimentally.[11] More recently, this was implemented in the KISSA framework to account for the influence of natural convection during pre-scan or pre-step rest times and/or in experiments involving would-be extended diffusion layers (i.e. t larger than a few seconds under usual electrochemical conditions involving classical electrolytes).[12]

It is clear that, under short-time ECL experimental conditions, natural convection may be negligible (overall duration of less than a few seconds). This is generally true for stepped potential ECL experiments, but may be incorrect for voltammetric ones. Indeed, to increase the exergonicity of the ET steps in Equations (3) or (7) required to generate visible photons, one needs to oppose two redox species with the largest difference (i.e. generally around a few volts) in standard potentials. Hence, scanning one wave voltammetrically and then another requires a time duration that may exceed a few seconds, so that the diffusion layer may well bump into the convective limit as the experiment is performed. On the other hand, our present simulation approach considers any limitation by natu-

[1] *Furthermore, ref. [18] reports theoretical predictions based on simulations and a fitting algorithm utilising Equation (11) of ref. [18], which appear to agree with the experimental results, but which we could not reproduce.*

ral convection intrinsically (although users may wish to disconnect this module). We thus now wish to address this effect based on a reported voltammetric investigation of an ECL annihilation system involving electron-donor-substituted phenylethynylanthronitriles, that is, compounds in which a series of single parent molecules may be oxidised or reduced at different sites.[19] The published reaction mechanism, summarised in Equations (19)–(23), was valid for four compounds of a series of six synthesised and investigated:

$$(A-D)+e \rightleftharpoons ({}^{\bullet-}A-D) \quad (20)$$

$$(A-D)-e \rightleftharpoons (A-D^{\bullet+}) \quad (21)$$

$$(A-D^{\bullet+})+({}^{\bullet-}A-D) \xrightarrow{k^{ET}} {}^{3}(A-D)^{*}+(A-D) \quad (22)$$

$${}^{3}(A-D)^{*}+{}^{3}(A-D)^{*} \xrightarrow{k^{T\rightarrow S}} (A-D)_2^{*} \quad (23)$$

$$(A-D)_2^{*} \xrightarrow{k^{ECL}} (A-D)_2+h\nu \quad (24)$$

$$(A-D)_2 \xrightarrow{k^{cleav}} 2(A-D) \quad (25)$$

This mechanism is formally akin to the general one given in Scheme 2b [with A = B = (A–D) and Eq. (9b) is split into the two sequential elementary steps in Eqs. (24) and (25)]. Although this mechanism is too idealistic because the experimental oxidation waves reported in ref. [19] have current peaks that are too small relative to their reduction counterparts (although this is supposed to be diffusion of the same compound) and are near chemically irreversible, we wish to use it to evaluate the effect of precision and illustrate the precision with which KISSA-1D is able to track the excimer species $(A-D)_2^{*}$ concentration profile automatically.

As reported in ref. [19], we consider that cyclic voltammetry (CV) experiments start through a cathodic scan, so that ${}^{\bullet-}A-D$ is produced initially and diffuses towards the solution bulk. Hence, only a part of it may be consumed while the backward scan extends to encompass the oxidation wave that generates $A-D^{\bullet+}$. The formation of the excimer species $(A-D)_2^{*}$ begins near the electrode surface with the onset of the oxidation wave because $A-D^{\bullet+}$ is then created and reacts immediately with remaining ${}^{\bullet-}A-D$ still present near the electrode surface, where it is continuously oxidised in this potential range. Although, as more $A-D^{\bullet+}$ is produced and more ${}^{\bullet-}A-D$ is consumed in Equation (22), $(A-D)_2^{*}$ is produced further and further into the solution, following displacement of the reaction front created by Equation (22) towards the bulk solution, since the excimer's short lifetime does not allow any significant diffusional spreading. This is illustrated in Figure 3a over a time window featuring a scan of the oxidation wave upon considering only pure diffusional transport. Figure 3b represents the corresponding time evolution of the simulation grid to establish that its mesh points automatically distribute near the reaction front, so that the concentration of the excimer species is tracked with high precision and accuracy despite its intrinsically very low concentration. Figure 3c represents the same variations of the $(A-D)_2^{*}$ concentration profile with time when natural convection is considered with an extension of 200 μm for the convection-free layer.[11,12] Natural

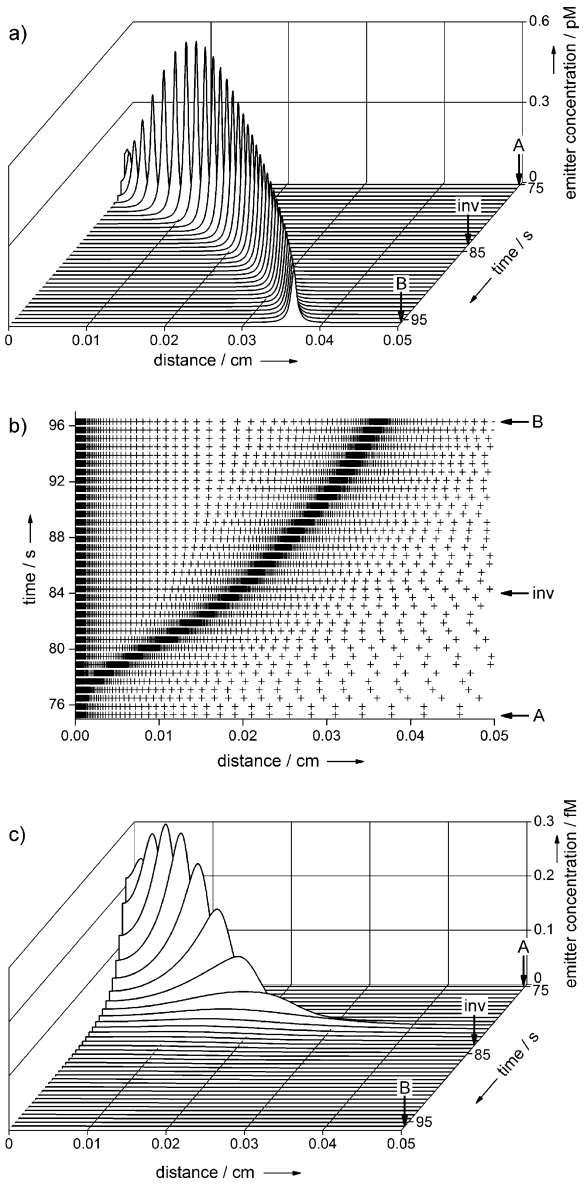

Figure 3. Concentration profiles of the excimer $(A-D)_2^{*}$ generated in the sequence of Equations (20)–(25) during a voltammetric scan ($\nu = 50\ mV\,s^{-1}$) in the absence (a) or in the presence (c) of natural convection when considering a convection-free layer of 200 μm; see text for the simulated experimental conditions. b) The spontaneous evolution of the simulation grid with time to automatically track the reaction front created by Equation (22), so that the $(A-D)_2^{*}$ concentration profile may be simulated with excellent precision and accuracy. The bulk concentration in simulations ($c^{bulk} = 10^{-4}$ M) was identical to that in ref. [19] and standard potentials [$E^0_{red} = -0.8914$ V and $E^0_{ox} = 1.5914$ V, respectively, for Eqs. (20) and (21) with heterogeneous rate constants equal to $1\ cm\,s^{-1}$ for both] were adjusted to match reported experimental peak potentials, while the values of diffusion coefficients ($D = 10^{-5}\ cm^2\,s^{-1}$) and rate constants were arbitrarily set to realistic values: $k^{ET} = 10^{10}\ M^{-1}\,s^{-1}$, $k^{S\rightarrow T} = 10^{8}\ M^{-1}\,s^{-1}$, $k^{ECL} = 10^{7}\ s^{-1}$ and $k^{cleav} = 10^{10}\ s^{-1}$. All potentials refer to the Ag/AgCl reference electrode. In all panels, only a fraction of the actual potential scan, that is, from $E_A = 1.35$ V (labelled "A") to $E_{inv} = 1.8$ V (labelled "inv") and back to $E_B = 1.18$ V (labelled "B"), is shown to focus on the range where the main ECL wave is observed. Only the portion of the diffusion layer of interest is shown in each panel (actual simulations were performed over the full diffusion layer thickness, namely, $6\sqrt{Dt_{max}}$). For clarity, in (b) all of the grid points in space are shown, but only for one out of every five time steps.

convection does not affect the system as much when the reduction wave is scanned because the time elapsed is too short. However, it has a pronounced effect on the concentration of $^{\bullet-}A-D$ present over the distances from the electrode that are of interest. Indeed, during the backward scan, performed after scanning the reduction wave, $^{\bullet-}A-D$ is, on the one hand, oxidised at the electrode and, on the other hand, expelled towards the bulk solution at a higher speed than in the absence of natural convection. As expected, the concentration of $(A-D)_2^*$ is not only greatly decreased (ca. 2000 times) and lasts for a shorter time, but, unexpectedly, is simultaneously confined to a more narrow range of solution near the electrode surface.

2.3. Simulation of ECL in the $[Ru(bpy)_3]^{2+}$/Tri-*n*-propylamine (TPrA) system

The discovery of ECL systems involving $[Ru(bpy)_3]^{2+}$ (bpy = 2,2′-bipyridine) and substituted alkyl amines, such as tripropylamine (TPrA), has been the subject of extensive mechanistic and development studies,[1] owing to their important applications in highly sensitive methods for immunoassays and DNA analyses. It is not our purpose to revisit the mechanistic validity of the results that have been published, but to illustrate that our approach can tackle very easily an extremely complex mechanism. For this purpose, we rely hereafter on a mechanism that includes all mechanistic paths considered in a recent investigation by Bard et al.[20] [Eqs. (26)–(36)].

In Scheme 3, Im^+ is the iminium product and DPrA is dipropylamine. With respect to ref. [20], we have added Equation (35), which apparently was not considered by the authors, but is necessary because Ru^{III} is a stronger oxidant than Ru^{II}.

The ECL response of this system is uncommon because it provides two distinct "ECL waves" due to three different mechanistic pathways, depending on the electrode potential, although in all three cases the only photon emitting species is $[Ru(bpy)_3]^{2+*}$. The most anodic ECL wave is observed when $[Ru(bpy)_3]^{2+}$ may be significantly oxidised at the electrode surface [Eq. (32)], so that $[Ru(bpy)_3]^{3+}$ may react with $[Ru(bpy)_3]^{+}$ [Eq. (34)] formed by a reaction between $TPrA^{\bullet}$ and $[Ru(bpy)_3]^{2+}$ [Eq. (29)], as well as with the $TPrA^{\bullet}$ radical itself [Eq. (35)] to generate the photon-emitting $[Ru(bpy)_3]^{2+*}$ species [Eq. (31)].[20] The less anodic ECL wave corresponds to two different kinetic controls that are mostly influenced by the relative concentrations of $TPrA^{\bullet}$ and $TPrA^{\bullet+}$ radicals versus that of $[Ru(bpy)_3]^{2+}$.[20]

Simulation of such complex kinetic behaviour thus requires extreme precision and accuracy to evaluate not only the time and space dependence of intermediate species concentrations (as above), but also to predict the above mechanistic shifts correctly as a function of potential and $[Ru(bpy)_3]^{2+}$ and TPrA bulk concentrations. In this sense, such a complex situation provides a good application example for our approach. Figure 4a shows that the experimental behaviour observed by Bard et al.[20] is readily reproduced through the display of the two ECL waves with their characteristic shapes and relative magnitudes; the first one reaches its comparatively low maximum plateau intensity before $[Ru(bpy)_3]^{2+}$ is significantly oxidised, whereas the second one displays a CV-like shape at higher potentials. Figure 4b and c confirms the previous mechanistic interpretations[20] through a comparison of the simulated concentration profiles of the four main species involved in the production of $[Ru(bpy)_3]^{2+*}$ at the first and second ECL waves, respectively. Being able to verify any tentative mechanistic interpretation based on such concentration profiles is then an important advantage of our present approach.

$$TPrAH^+ \rightleftharpoons TPrA + H^+, \quad pKa = 10.4 \tag{26}$$

$$TPrA - e \rightleftharpoons TPrA^{\bullet+}, \quad k^0_{TPrA0/+}, E^0_{TPrA0/+} \tag{27}$$

$$TPrA^{\bullet+} \rightleftharpoons TPrA^{\bullet} + H^+, \quad k_f^{TPrA^{\bullet}}, K_{eq}^{TPrA^{\bullet}} \tag{28}$$

$$TPrA^{\bullet} + Ru(bpy)_3^{2+} \rightleftharpoons Im^+ + Ru(bpy)_3^{+}, \quad k_f^1, K_{eq}^1 \tag{29}$$

$$TPrA^{\bullet+} + Ru(bpy)_3^{+} \rightleftharpoons TPrA + Ru(bpy)_3^{2+*}, \quad k_f^2, K_{eq}^2 \tag{30}$$

$$Ru(bpy)_3^{2+*} \rightarrow Ru(bpy)_3^{2+} + h\nu, \quad k_f^{ECL} \tag{31}$$

$$Ru(bpy)_3^{2+} - e \rightleftharpoons Ru(bpy)_3^{3+}, \quad k^0_{Ru2+/3+}, E^0_{Ru2+/3+} \tag{32}$$

$$Ru(bpy)_3^{+} - e \rightleftharpoons Ru(bpy)_3^{2+}, \quad k^0_{Ru+/2+}, E^0_{Ru+/2+} \tag{33}$$

$$Ru(bpy)_3^{3+} + Ru(bpy)_3^{+} \rightarrow Ru(bpy)_3^{2+} + Ru(bpy)_3^{2+*}, \quad k^{ET} \tag{34}$$

$$TPrA^{\bullet} + Ru(bpy)_3^{3+} \rightleftharpoons Im^+ + Ru(bpy)_3^{2+*}, \quad k_f^3, K_{eq}^3 \tag{35}$$

$$Im^+ \xrightarrow{+H_2O} (CH_3)_2CO + DPrA, \quad k_{hydrol} \tag{36}$$

Scheme 3.

3. Computations by KISSA-1D

KISSA[9] software was developed by us by using the Embarcadero Delphi XE3 program development environment. All simulations quoted herein were performed on a PC with an Intel Core-i7 processor at 2.2 GHz. Due to the adaptive nature of the computational spatial grids employed, simulation times strongly depend on the reaction rates involved.[9,12,13,22] To enhance the stability and efficiency of calculations, an original algorithm was also designed to refine the time grid (different from that implemented in the ECL Package)[2,3] when the conditions at the electrode surface changed very rapidly (e.g. during step potential excitation). Thus, for the reaction mechanisms reported herein (i.e. assuming the rate constants of second-order reactions to be at the diffusion limit, namely, $\approx 10^{10}\ M^{-1}\ s^{-1}$), depending on particular transient conditions automatically generated computational grids consisted of 100 to 350 nodes, while simulation times did not exceed 10 s [or 20 s for the mechanism of the reactions given in Eqs. (26)–(36) due to a large number of reactions and species] when 2000 time steps were used in each case.

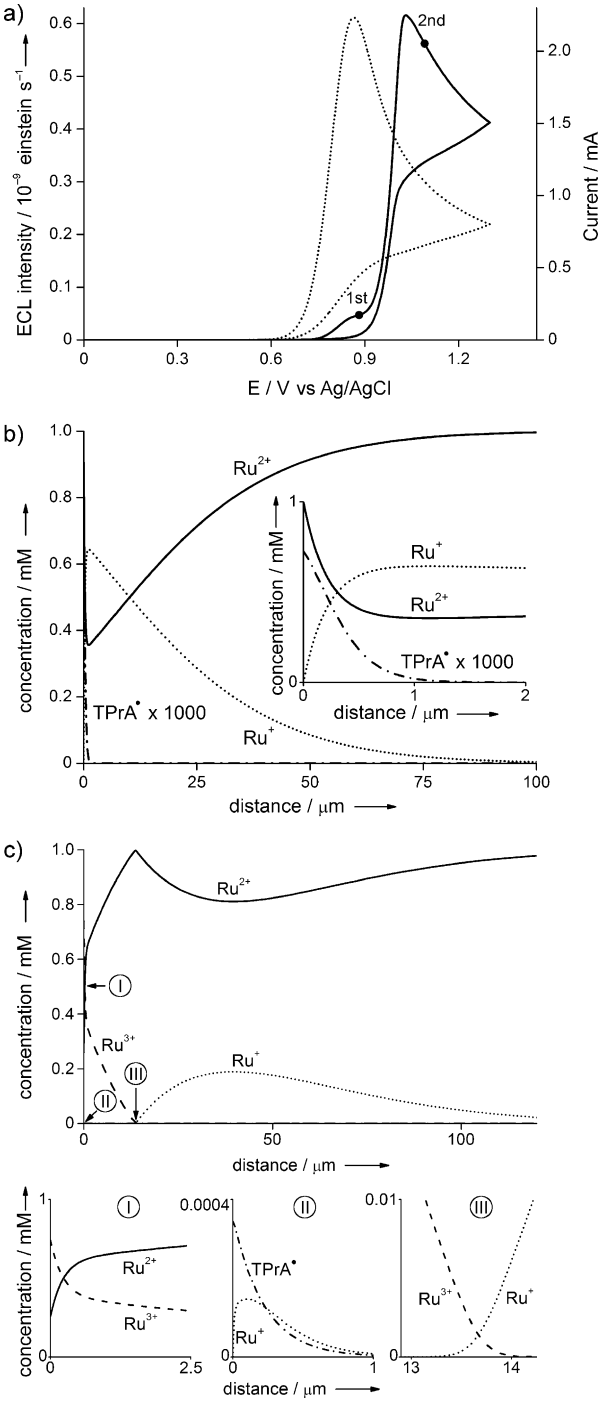

Figure 4. a) Simulated ECL intensity (solid line) and voltammogram (dotted line) at $v = 0.1\,V\,s^{-1}$ for the $[Ru(bpy)_3]^{2+}$/TPrA system for $[Ru(bpy)_3]^{2+} = 1\,mM$ and $[TPrA] = 0.1\,M$ under conditions (pH buffered at 8.5) similar to those reported in ref. [20]. Concentration profiles at the first, $E = 0.88\,V$ (b), or second, $E = 1.09\,V$ (c), ECL waves: $[Ru(bpy)_3]^{2+}$ (solid line), $[Ru(bpy)_3]^{3+}$ (dashed line), $[Ru(bpy)_3]^{+}$ (dotted line) and TPrA$^{\bullet}$ (dashed-dotted line). Some thermodynamic values ($E^0_{TPrA0/+} = 0.88\,V$, $E^0_{Ru2+/3+} = 1.06\,V$, $E^0_{Ru+/2+} = -1.48\,V$, $K^{TPrA^{\bullet}}_{eq} = 0.05\,M$) and diffusion coefficients ($D_{TPrA} = D_{TPrAH^+} = D_{TPrA^{\bullet+}} = D_{TPrA^{\bullet}} = 5 \times 10^{-6}\,cm^2\,s^{-1}$, $D_{Ru^+} = D_{Ru^{2+}} = D_{Ru^{3+}} = D_{Ru^{2+*}} = 5 \times 10^{-6}\,cm^2\,s^{-1}$, $D_{H^+} = 5 \times 10^{-5}\,cm^2\,s^{-1}$, $D_{P_1} = D_{P_2} = 5 \times 10^{-5}\,cm^2\,s^{-1}$) were taken from ref. [20], whereas the others ($k_f^{TPrA^{\bullet}} = 10^4\,s^{-1}$, $k_f^1 = 10^{10}\,M^{-1}\,s^{-1}$, $K^1_{eq} = 10^{10}$, $k_f^2 = 10^6\,M^{-1}\,s^{-1}$, $K^2_{eq} = 10^7$, $k_f^{ECL} = 10^8\,s^{-1}$, $k_{P1} = 10^7\,s^{-1}$, $k^{ET} = 10^{10}\,M^{-1}\,s^{-1}$, $k^0_{TPrA0/+} = 0.01\,cm\,s^{-1}$, $k^0_{Ru2+/3+} = 1\,cm\,s^{-1}$, $k^0_{Ru+/2+} = 1\,cm\,s^{-1}$) were adjusted to obtain a behaviour of the ECL intensity and CV curves coherent with the data published in ref. [20]. All potentials refer to the Ag/AgCl reference electrode.

4. Conclusions

This work aims to introduce a novel computational approach that is easy to use and allows stable, precise and efficient simulation of any complex reaction mechanisms driven electrochemically without relying on extensive computational time and memory occupation. One great merit of this approach is extremely precise prediction of time dependence of concentration profiles for any intermediates, including exceedingly transient ones of vanishingly low concentration, as occurrs in any electrochemical mechanism leading to ECL emission. Indeed, in such mechanisms that are of great interest for modern physicochemical or bioanalytical applications, photon-emitting species are highly reactive species formed and evolving at rates that dwarf most usual ones, so that their concentrations, albeit crucial for the ECL intensity, are vanishingly small. The extreme performance of the proposed approach stems from the integration of specific conformal maps to track any severe constraint imposed by diffusional transport with a new kinetic criterion,[9a] which specifically guides local adaptation in the conformal space,[9d] to track and solve any kinetic difficulty present at any position in the diffusion layer. This allows the numerical treatment of rate constants up to values that may greatly exceed any physically realistic ones. The definition of this criterion is based on the value of the kinetic terms themselves, so that its application does not need a pre-integration step or iterations, as commonly performed in finite difference approaches dealing with high-rate linear or non-linear chemical kinetics. This is crucial for most kinetic situations encountered in ECL systems.

We established that KISSA-1D, developed on the basis of this approach, produces numerical solutions that are in excellent agreement with the corresponding analytical values derived in this work for ECL conditions, which could be considered as the ultimate ones for such systems. Very good agreement was also found with numerical results obtained by an independent approach implemented in Comsol. Therefore, these tests validated the accuracy and precision of predictions based on KISSA-1D in most generally softer conditions encountered experimentally.

The performance of KISSA-1D was illustrated through considering a series of published ECL reaction schemes that encompas most of the ECL systems reported to date. This performance does not require any particular computer or mathematical skills on part of the user. Indeed, it is associated with an easy definition of the reaction schemes to be solved, since they are entered in conventional chemical format and the above conformal mapping and kinetic criterion are completely invisible to users (unless they wish to observe them, as illustrated in Figure 3 b). Also, concentration profiles of any species involved at any time of a simulated experiment may be directly accessed to stimulate users into proposing quantitative rationalisation of observed overall behaviour or to sustain/disprove their interpretation. Finally, when users wish to do so, the approach may incorporate a treatment of spontaneous convection, again a transparent feature. Indeed, this phenomenon may be critical under some conditions, such as during

long experiments or involving long rest times, as in voltammetrically induced annihilation ECL mechanisms, because then the system transport equations or initial conditions cannot be described by diffusion only (compare Figure 3a and c).

We believe that all of these features provide a series of important advantages to non-mathematically oriented electrochemical users. This is particularly true when compared with existing software and approaches. Indeed, even if non-specialised simulation software, such as Comsol,[6] may provide numerical results with similar precision and accuracy (as shown herein, see Figure 2), this is at the expense of longer computation times and the necessity of entering complex mathematical equations in non-analytical formulation to define reaction schemes and electrochemical boundary conditions owing to their specificity.

Analytical Solutions

A1. Analytical Solutions for Annihilation-Type ECL in Scheme 1 [Eqs. (1)–(4)]

Firstly, consider Scheme 1 for annihilation ECL given in Equations (1)–(4). Suppose that initially (at $t = 0$) the solution is fully electrolysed, so that it contains the oxidised form of luminophore species A exclusively (e.g. after an infinitely long anodic pulse). At $t = 0$, a positive potential pulse is applied to the electrode, so that all ET steps and the bimolecular reaction [Eq. (3)] proceed under diffusion control, while the emission step [Eq. (4)] has a finite rate defined by the first-order rate constant k^{ECL}. Additionally, we assume that, at the potential of the anodic pulse, the excited state is oxidised under diffusion control [Eq. (A1.1)]:

$$A^* - e \rightarrow A^+ \tag{A1.1}$$

This hypothetical situation allows us to illustrate the accuracy and efficiency of the simulation approach implemented in KISSA-1D when applied to ECL systems.

Let us assume that all reacting species have the same diffusivities and introduce the dimensionless parameters given in Equation (A1.2):

$$\tau = \frac{t}{t_{max}},\ y = \frac{x}{\sqrt{Dt_{max}}},\ K^* = k^{ECL}t_{max},\quad a^- = \frac{[A^-]}{c_0},\ a^+ = \frac{[A^+]}{c_0},\ a^* = \frac{[A^*]}{c_0} \tag{A1.2}$$

in which x is the distance from the electrode surface, t is the time, D is the diffusion coefficient, t_{max} is the duration of the potential step and c_0 is the bulk concentration of A.

Because species A^+ and A^- cannot coexist in bulk solution due to their infinite reactivity with each other, the bulk solution can be naturally subdivided into two regions separated by the moving front of the reaction given in Equation (3) located at $y = \mu(\tau)$.[17,22] Then, in zone I, adjacent to the electrode ($0 < y < \mu(\tau)$) Equations (A1.3)–(A1.5) are valid:

$$a^- \equiv 0 \tag{A1.3}$$

$$\frac{\partial a^+}{\partial \tau} = \frac{\partial^2 a^+}{\partial y^2} \tag{A1.4}$$

$$\frac{\partial a^*}{\partial \tau} = \frac{\partial^2 a^*}{\partial y^2} - K^* a^* \tag{A1.5}$$

In zone II ($\mu(\tau) < y < \infty$), concentration distributions satisfy Equations (A1.6)–(A1.8):

$$a^+ \equiv 0 \tag{A1.6}$$

$$\frac{\partial a^-}{\partial \tau} = \frac{\partial^2 a^-}{\partial y^2} \tag{A1.7}$$

$$\frac{\partial a^*}{\partial \tau} = \frac{\partial^2 a^*}{\partial y^2} - K^* a^* \tag{A1.8}$$

The boundary conditions are given in Equation (A1.9):

$$y = 0:\ a^+ = 1 \tag{A1.9a}$$

$$a^* = 0 \tag{A1.9b}$$

$$y = \mu(\tau):\ a^- = a^+ = 0 \tag{A1.9c}$$

$$a^*(\mu - 0, \tau) = a^*(\mu + 0, \tau) \tag{A1.9d}$$

$$\left.\frac{\partial a^+}{\partial y}\right|_{y=\mu-0} = -\left.\frac{\partial a^-}{\partial y}\right|_{y=\mu+0} \tag{A1.9e}$$

$$-\varepsilon\left.\frac{\partial a^+}{\partial y}\right|_{y=\mu-0} = \left.\frac{\partial a^*}{\partial y}\right|_{y=\mu-0} - \left.\frac{\partial a^*}{\partial y}\right|_{y=\mu+0} \tag{A1.9f}$$

$$y = \infty:\ a^+ = 0,\ a^- = 1,\ a^* = 0 \tag{A1.9g}$$

The solution for the concentrations of species A^+ and A^- can be found in the same manner as that for the EE system[22] to yield Equations (A1.10) and (A1.11):

$$a^+(y, \tau) = 1 - 2\mathrm{erf}\left(\frac{y}{2\sqrt{\tau}}\right),\ 0 < y < \mu(\tau) \tag{A1.10}$$

$$a^-(y, \tau) = 1 - 2\mathrm{erfc}\left(\frac{y}{2\sqrt{\tau}}\right),\ \mu(\tau) < y < \infty \tag{A1.11}$$

The reaction front position is then defined by Equation (A1.12):

$$\mu(\tau) = 2\eta\sqrt{\tau} \tag{A1.12}$$

in which constant η is found from $\mathrm{erf}(\eta) = 1/2$ (namely, $\eta \approx 0.476936$).

Partial differential Equations (A1.5) and (A1.8), describing the concentration distribution of the emitter species, cannot be solved to yield a closed-form analytical solution. However, analytical solutions can be found for limiting situations corresponding to short and long times.

Let us first consider the long time limit. When the reaction front of the bimolecular reaction in Equation (3) has travelled sufficiently far from the electrode surface for the ET reaction in

Equation (A1.1) to have a negligible effect on the concentration distribution of A* (namely, when the reaction layer thickness $\sim 1/\sqrt{K^*}$ is much smaller than that of μ), Equations (A1.5) and (A1.8) can be considered in the pure kinetic limit,[14] when the concentration distribution, a^*, is quasi-steady around the reaction front. Under these conditions, we seek the solution of Equation (A1.13)

$$\frac{\partial^2 a^*}{\partial y^2} = K^* a^* \tag{A1.13}$$

satisfying Equations (A1.9b), (A1.9d), (A1.9f) and (A1.9g).

The general solution of Equation (A1.13) has the form of Equation (A1.14):

$$a_i^*(y) = A_i e^{-\sqrt{K^*}y} + B_i e^{\sqrt{K^*}y} \tag{A1.14}$$

with unknown coefficients A_i and B_i (the index i refers to the zone of space where the equation is considered).

Applying the boundary condition in Equation (A1.9b) reduces the solution in zone I to Equation (A1.15):

$$a_I^*(y) = A_I \sinh\left(\sqrt{K^*}y\right) \tag{A1.15}$$

while applying the condition in Equation (A1.9g) at infinity yields the solution in zone II in the form of Equation (A1.16):

$$a_{II}^*(y) = A_{II} e^{-\sqrt{K^*}y} \tag{A1.16}$$

Applying the continuity condition [Eq. (A1.9d)] provides the relationship between coefficients A_I and A_{II} in Equation (A1.17):

$$A_{II} = A_I \frac{\sinh\left(\sqrt{K^*}\mu\right)}{e^{-\sqrt{K^*}\mu}} \tag{A1.17}$$

Finally, substituting the derivatives of Equations (A1.10), (A1.15) and (A1.16) into Equation (A1.9f), which imposes flux conservation, yields Equation (A1.18):

$$A_I = \frac{2\varepsilon}{\sqrt{\pi K^* \tau}} e^{-\eta^2 - \sqrt{K^*}\mu} \tag{A1.18}$$

so that the final solutions in zones I and II are those given in Equations (A1.19) and (A1.20):

$$a_I^*(y) = \frac{2\varepsilon}{\sqrt{\pi K^* \tau}} e^{-\eta^2 - 2\eta\sqrt{K^*\tau}} \sinh\left(\sqrt{K^*}y\right) \tag{A1.19}$$

$$a_I^*(y) = \frac{2\varepsilon}{\sqrt{\pi K^* \tau}} e^{-\eta^2} \sinh\left(2\eta\sqrt{K^*\tau}\right) e^{-\sqrt{K^*}y} \tag{A1.20}$$

The ECL intensity is proportional to the instantaneous quantity of the emitter in the whole bulk solution [Eq. (A1.21)]:

$$I_{ECL}(\tau) = \gamma k^{ECL} c_0 S \sqrt{D t_{max}} \int_0^\infty a^* dy \tag{A1.21}$$

in which S is the electrode surface area.

The integral in Equation (A1.21) is evaluated as Equation (A1.22):

$$\int_0^\infty a^* dy = \int_0^{2\eta\sqrt{\tau}} a_I^* dy + \int_{2\eta\sqrt{\tau}}^\infty a_{II}^* dy = \frac{2\varepsilon}{\sqrt{\pi K^* \tau}} e^{-\eta^2}\left(1 - e^{-2\eta\sqrt{K^*\tau}}\right) \tag{A1.22}$$

Subsequently, we use the dimensionless ECL intensity defined in Equation (A1.23):

$$\psi_{ECL}^{long} = \frac{I_{ECL}}{2\varepsilon\gamma c_0 S\sqrt{Dk^{ECL}}} = \frac{1}{\sqrt{\pi\theta}} e^{-\eta^2}\left(1 - e^{-2\eta\sqrt{\theta}}\right) \tag{A1.23}$$

in which the scaled dimensionless time is defined as $\theta = k^{ECL} t$.

The short time limit of the concentration distribution of the emitter can be obtained by taking into account that, at initial time moments, the rate of production of A* (which is proportional to the flux, namely, $\sim 1/\sqrt{\tau}$) is much higher than the rate of its emissive decay (proportional to the quantity of emitter generated, namely, $\sim \sqrt{\tau}$). Then, the reaction terms in Equations (A1.5) and (A1.8) can be ignored and the solution can then be obtained in the form of Equations (A1.24) and (A1.25):

$$a_I^*(y,\tau) = \varepsilon \ \mathrm{erf}\left(\frac{y}{2\sqrt{\tau}}\right) \tag{A1.24}$$

$$a_{II}^*(y,\tau) = \varepsilon \ \mathrm{erfc}\left(\frac{y}{2\sqrt{\tau}}\right) \tag{A1.25}$$

Evaluating the ECL intensity according to Equation (A1.21) and normalising it, as in Equation (A1.23), we obtain Equation (A1.26) for short times:

$$\psi_{ECL}^{short} = \frac{I_{ECL}}{2\varepsilon\gamma c_0 S\sqrt{Dk^{ECL}}} = \left(2e^{-\eta^2} - 1\right)\sqrt{\frac{\theta}{\pi}} \tag{A1.26}$$

A2. Analytical Solutions for Co-reactant-Type ECL in Scheme 2 [Eqs. (5)–(9)]

Let us consider the reaction mechanism in Equations (5)–(8a) and (9a), leading to ECL emission through the formation of a triplet intermediate, which then produces a singlet excited state through a second-order reaction. The triplet and singlet species are assumed to be oxidisable at the same potentials as the initial species A.

Let us assume that initially the solution contains only the reduced form of species B (namely, after exhaustive electrolysis) and species A in its ground state at equal concentrations of c_0. The application of an anodic pulse at $t = 0$ drives the reaction

given in Equation (5) under diffusion control, thus initiating the whole reaction cascade given in Equations (7), (8a) and (9a) to produce the excited state and ECL emission upon its return to the ground state. In the following we derive limiting analytical solutions for short and long times by assuming extremely large values of rate constants k^{ET} and k^{ECL}, so that the system dynamics are controlled by the kinetics of the reaction given in Equation (8a).

By introducing the dimensionless parameters given in Equation (A2.1):

$$\tau = k^{T\to S}c_0 t, \quad y = x\sqrt{\frac{k^{T\to S}c_0}{D}}, \quad a^+ = \frac{[A^+]}{c_0}, \quad b^- = \frac{[B^-]}{c_0}, \quad a^* = \frac{[A^*]}{c_0} \tag{A2.1}$$

one can formulate the problem in the form given in Equations (A2.2)–(A2.4) [taking into account the natural subdivision of space into two zones due to the fast reaction given in Equation (7) as in the annihilation case considered in Section A1]:

Zone I, $0 < y < \mu(\tau)$:

$$\frac{\partial a^+}{\partial \tau} = \frac{\partial^2 a^+}{\partial y^2} \tag{A2.2}$$

$$\frac{\partial a_3}{\partial \tau} = \frac{\partial^2 a_3}{\partial y^2} - 2a_3^2 \tag{A2.3}$$

$$b^- \equiv 0 \tag{A2.4}$$

Zone II, $\mu(\tau) < y < \infty$:

$$\frac{\partial b^-}{\partial \tau} = \frac{\partial^2 b^-}{\partial y^2} \tag{A2.5}$$

$$\frac{\partial a_3}{\partial \tau} = \frac{\partial^2 a_3}{\partial y^2} - 2a_3^2 \tag{A2.6}$$

$$a^+ \equiv 0 \tag{A2.7}$$

The boundary conditions are given in Equation (A2.8):

$$y = 0: \quad a^+ = 1 \tag{A2.8a}$$

$$a_3 = 0 \tag{A2.8b}$$

$$y = \mu(\tau): \quad a^+ = b^- = 0 \tag{A2.8c}$$

$$\left.\frac{\partial b^-}{\partial y}\right|_{y=\mu+0} = -\left.\frac{\partial a^+}{\partial y}\right|_{y=\mu-0} \tag{A2.8d}$$

$$a_3(\mu - 0, \tau) = a_3(\mu + 0, \tau) \tag{A2.8e}$$

$$\left.\frac{\partial a_3}{\partial y}\right|_{y=\mu-0} - \left.\frac{\partial a_3}{\partial y}\right|_{y=\mu+0} = -\varepsilon\left.\frac{\partial a^+}{\partial y}\right|_{y=\mu-0} \tag{A2.8f}$$

$$\left.\frac{\partial a_3}{\partial y}\right|_{y=\mu-0} = -\left.\frac{\partial a_3}{\partial y}\right|_{y=\mu+0} \tag{A2.8g}$$

$$y = \infty: \quad a^+ = 0, \; b^- = 0, \; a_3 = 0 \tag{A2.8h}$$

Note that Equation (A2.8e) implies continuity of the concentration distribution of A^{3*}, while Equation (A2.8f) imposes the rate of production of this species and Equation (A2.8g) indicates equal rates of diffusion of A^{3*} away from the reaction front.

Proceeding in the same way as that described in Section A1 for the annihilation-type ECL in Scheme 1, we can write solutions for a^+ and b^- in zones I and II, as Equations (A2.9) and (A2.10), respectively:

$$a^+(y,\tau) = 1 - 2\mathrm{erf}\left(\frac{y}{2\sqrt{\tau}}\right), \; 0 < y < \mu(\tau), \tag{A2.9}$$

$$b^-(y,\tau) = 1 - 2\mathrm{erfc}\left(\frac{y}{2\sqrt{\tau}}\right), \; \mu(\tau) < y < \infty, \tag{A2.10}$$

with the reaction front position defined by Equation (A2.13).

To obtain the long time solution for the concentration of the triplet, A^{3*}, let us consider Equations (A2.3) and (A2.6) in their pure kinetic limit [Eq. (A2.11)]:

$$\frac{\partial^2 a_3}{\partial y^2} = 2a_3^2 \tag{A2.11}$$

The general solution of Equation (A2.11) is given by Equation (A2.12):

$$a_3(y) = \sqrt[3]{3}\,\wp\left(\frac{y + C_1}{\sqrt[3]{3}}, \; 0, \; C_2\right) \tag{A2.12}$$

in which $\wp(z, g_2, g_3)$ is the Weierstrass' elliptic function;[23] C_1 and C_2 are constants. Because $a_3(\infty) = 0$, it follows that $C_2 = 0$ (i.e. both periods of the doubly periodic function, $\wp$, are infinite)[23] and the solution in zone II reduces to Equation (A2.13):

$$a_3^{II}(y) = \frac{3}{(y + C_1^{II})^2} \tag{A2.13}$$

Substituting the derivatives of expressions in Equations (A2.9) and (A2.13) into Equation (A2.8f) and taking into account Equation (A2.8g), we obtain the following expression for C_1^{II} [Eq. (A2.14)]:

$$C_1^{II} = \left[\frac{6\sqrt{\pi\tau}}{\varepsilon}e^{\eta^2}\right]^{1/3} - 2\eta\sqrt{\tau} \tag{A2.14}$$

so that the triplet concentration in zone II is given by Equation (A2.15):

$$a_3^{II}(y) = 3\left(y - 2\eta\sqrt{\tau} + \left[\frac{6\sqrt{\pi\tau}}{\varepsilon}e^{\eta^2}\right]^{1/3}\right)^{-2} \tag{A2.15}$$

At sufficiently long times, the solution in zone I can also be presented in the form given in Equation (A2.13). Because the concentration of A^{3*} decays as y^{-2} away from the reaction

front, the zero-concentration condition in Equation (A2.8b) at the electrode surface is satisfied with an accuracy of better than 2% (relative to the concentration of A^{3*} at the reaction front itself) for $\tau > 50$. Substitution of boundary conditions in Equations (A2.8f) and (A2.8g) yields Equations (A2.16) and (A2.17):

$$C_1^{\mathrm{I}} = -\left[\frac{6\sqrt{\pi\tau}}{\varepsilon}e^{\eta^2}\right]^{1/3} - 2\eta\sqrt{\tau} \tag{A2.16}$$

$$a_3^{\mathrm{I}}(y) \approx 3\left(y - 2\eta\sqrt{\tau} - \left[\frac{6\sqrt{\pi\tau}}{\varepsilon}e^{\eta^2}\right]^{1/3}\right)^{-2} \tag{A2.17}$$

The intensity of the ECL emission is then given by Equation (A2.18):

$$I_{\mathrm{ECL}} = \chi\gamma S k^{\mathrm{T}\to\mathrm{S}} c_0^2 \sqrt{\frac{D}{k^{\mathrm{T}\to\mathrm{S}} c_0}}\left[\int_0^{2\eta\sqrt{\tau}} \left(a_3^{\mathrm{I}}\right)^2 dy + \int_{2\eta\sqrt{\tau}}^{\infty} \left(a_3^{\mathrm{II}}\right)^2 dy\right] \tag{A2.18}$$

Upon normalising and evaluating the integrals, we obtain Equation (A2.19):

$$\psi_{\mathrm{ECL}}^{\mathrm{intermediate}} = \frac{I_{\mathrm{ECL}}}{\varepsilon\chi\gamma S c_0\sqrt{k^{\mathrm{T}\to\mathrm{S}} c_0 D}} = \frac{e^{-\eta^2}}{\sqrt{\pi\tau}} - 3\left(2\eta\varepsilon^{1/3}\sqrt{\tau} + \left[6\sqrt{\pi\tau}\,e^{\eta^2}\right]^{1/3}\right)^{-3} \tag{A2.19}$$

Note that as $\tau \to \infty$, Equation (A2.19) tends to Equation (A2.20)

$$\psi_{\mathrm{ECL}}^{\infty} = \frac{e^{-\eta^2}}{\sqrt{\pi\tau}} \tag{A2.20}$$

We now consider the short time limit. Similarly to the case of Scheme 1, the solution for the triplet species is obtained as Equations (A2.21) and (A2.22):

$$a_3^{\mathrm{I}}(y,\tau) = \varepsilon\,\mathrm{erf}\left(\frac{y}{2\sqrt{\tau}}\right) \tag{A2.21}$$

$$a_3^{\mathrm{II}}(y,\tau) = \varepsilon\,\mathrm{erfc}\left(\frac{y}{2\sqrt{\tau}}\right) \tag{A2.22}$$

Substituting these expressions into Equation (A2.18) and normalising the ECL intensity as in Equation (A2.19), we obtain Equation (A2.23):

$$\psi_{\mathrm{ECL}}^{\mathrm{short}} = 2\left[\int_0^{\eta} \mathrm{erf}^2(x)\mathrm{d}x + \int_{\eta}^{\infty} \mathrm{erfc}^2(x)\mathrm{d}x\right]\sqrt{\tau} = 0.2018\sqrt{\tau} \tag{A2.23}$$

Note that the reaction mechanism in Equations (5)–(7), (8b) and (9b), involving triplet dimerisation, follows the same limiting regimes as those obtained for the mechanism in Equations (5)–(7), (8a) and (9a).

Acknowledgements

This work has been supported in part by the CNRS (UMR 8640), Ecole Normale Superieure (ENS, Paris), University Pierre and Marie Curie (UPMC), and the French Ministry of Research. We thank ANR (Chaire d'Excellence project "MicroNanoChem") and CNRS for financial support of this project in ENS (UMR 8640). We thank also the State Fund for Fundamental Researches (Ukraine) and CNRS (France) for a PICS program. I.S. thanks Prof. Wujian Miao (University of Southern Mississippi) for stimulating discussions at the beginning of this work.

Keywords: adaptive computational grid · analytical solutions · electrochemiluminescence · kinetic criterions · KISSA software simulation

[1] a) A. J. Bard, L. R. Faulkner, *Electrochemical Methods: Fundamentals and Applications, 2nd ed.*, Wiley, New York, **2001**; b) W. Miao, *Chem. Rev.* **2008**, *108*, 2506–2553; c) X.-B. Yin, S. Dong, E. Wang, *TrAC Trends Anal. Chem.* **2004**, *23*, 432–441; d) R. Pyati, M. M. Richter, *Annu. Rep. Prog. Chem. Sect. C* **2007**, *103*, 12–78.
[2] I. B. Svir, A. I. Oleinick, A. V. Klimenko, *J. Electroanal. Chem.* **2001**, *513*, 119–125.
[3] I. B. Svir, A. I. Oleinick, *J. Electroanal. Chem.* **2001**, *499*, 30–38.
[4] C. Amatore, *Electrochemistry at Ultramicroelectrodes in Physical Electrochemistry: Principles, Methods and Applications* (Ed.: I. Rubinstein), Marcel Dekker, New York, **1995**, Chap. 4, pp. 131–208.
[5] a) M. Rudolph, D. P. Reddy, S. W. Feldberg, *Anal. Chem.* **1994**, *66*, A589–A600; b) J. B. Ketter, S. P. Forry, R. M. Wightman, S. W. Feldberg, *Electrochem. Solid-State Lett.* **2004**, *7*, E18–E22.
[6] Comsol Multiphysics, COMSOL, Inc., Burlington, MA.
[7] I. J. Cutress, E. J. F. Dickinson, R. G. Compton, *J. Electroanal. Chem.* **2010**, *638*, 76–83.
[8] M. M. Sartin, C. Shu, A. J. Bard, *J. Am. Chem. Soc.* **2008**, *130*, 5354–5360.
[9] a) C. Amatore, O. V. Klymenko, I. Svir, *Electrochem. Commun.* **2010**, *12*, 1170–1173; b) C. Amatore, O. V. Klymenko, I. Svir, *Electrochem. Commun.* **2010**, *12*, 1165–1169; c) O. V. Klymenko, A. Oleinick, I. Svir, C. Amatore, *Russ. J. Electrochem.* **2012**, *48*, 593–599; d) O. V. Klymenko, I. Svir, A. Oleinick, C. Amatore, *ChemPhysChem* **2012**, *13*, 845–859.
[10] C. Amatore, O. V. Klymenko, I. Svir, *Electrochim. Acta* **2011**, *56*, 4422–4423.
[11] a) C. Amatore, S. Szunerits, L. Thouin, J.-S. Warkocz, *J. Electroanal. Chem.* **2001**, *500*, 62–70; b) C. Amatore, S. Szunerits, L. Thouin, J. S. Warkocz, *Electroanalysis* **2001**, *13*, 646–652; c) C. Amatore, C. Pebay, O. Scialdone, S. Szunerits, L. Thouin, *Chem. Eur. J.* **2001**, *7*, 2933–2939; d) N. Baltes, L. Thouin, C. Amatore, J. Heinze, *Angew. Chem.* **2004**, *116*, 1455–1459; *Angew. Chem. Int. Ed.* **2004**, *43*, 1431–1435; e) C. Amatore, K. Knobloch, L. Thouin, *J. Electroanal. Chem.* **2007**, *601*, 17–28.
[12] C. Amatore, O. V. Klymenko, I. Svir, *Anal. Chem.* **2012**, *84*, 2792–2798.
[13] O. V. Klymenko, I. Svir, C. Amatore, *J. Electroanal. Chem.* **2013**, 688, 320–327.
[14] a) C. Amatore, J.-M. Savéant, *J. Electroanal. Chem.* **1977**, *85*, 27–46; b) C. Amatore in *Organic Electrochemistry* (Eds.: M. Baizer, H. Lund), Marcel Dekker, New York, **1991**, Chap. 2, pp. 11–119.
[15] S. W. Feldberg, *J. Am. Chem. Soc.* **1966**, *88*, 390–393.
[16] R. P. Van Duyne, S. F. Fischer, *Chem. Phys.* **1974**, *5*, 183–197.
[17] L. R. Faulkner, *J. Electrochem. Soc.* **1977**, *124*, 1724–1728.
[18] P. R. Michael, L. R. Faulkner, *J. Am. Chem. Soc.* **1977**, *99*, 7754–7761.
[19] A. Elangovan, K.-M. Kao, S.-W. Yang, Y.-L. Chen, T.-I. Ho, Y. O. Su, *J. Org. Chem.* **2005**, *70*, 4460–4469.
[20] W. Miao, J.-P. Choi, A. J. Bard, *J. Am. Chem. Soc.* **2002**, *124*, 14478–14485.

[21] L. R. Faulkner, A. J. Bard, *Electroanalytical Chemistry, Vol. 10* (Ed.: A. J. Bard), Marcel Dekker, New York, **1977**, pp. 1 – 95.
[22] O. V. Klymenko, I. Svir, C. Amatore, *Electrochem. Commun.* **2010**, *12*, 1378 – 1382.
[23] M. Abramowitz, I. A. Stegun, *Handbook of Mathematical Functions, 10th ed.*, U.S. National Bureau of Standards, Washington, D.C. **1972**.

Received: February 5, 2013
Published online on ■■ ■■, 2013

ARTICLES

Now you can predict even ECL: Fast and accurate prediction and treatment of electrochemiluminescence (ECL) reactions for any complex system is now possible owing to a new numerical approach implemented in KISSA software.

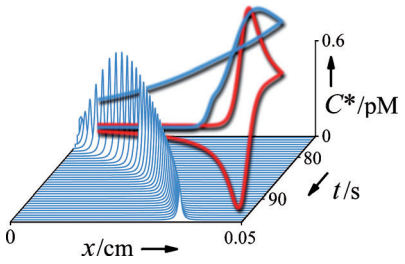

O. V. Klymenko, I. Svir, C. Amatore**

■■ – ■■

A New Approach for the Simulation of Electrochemiluminescence (ECL)